PCCP

ROYAL SOCIETY OF CHEMISTRY

PAPER

View Article Online
View Journal | View Issue

Cite this: *Phys. Chem. Chem. Phys.*, 2022, **24**, 9936

Metavalent bonding in chalcogenides: DFT-chemical pressure approach†

Hussien Helmy Hassan Osman *[ab] and Francisco Javier Manjón [b]

Received 25th February 2022,
Accepted 9th April 2022

DOI: 10.1039/d2cp00954d

rsc.li/pccp

Understanding the chemical bond nature has attracted considerable attention as it is crucial to analyze and comprehend the different physical and chemical properties of materials. This work is considered a complementary part of our previous work in studying the nature of different types of bonding interactions in a wide variety of molecules and materials using the DFT Chemical Pressure (CP) approach. Recently, a new type of chemical bond, the metavalent bond (MVB), has been defined. We show how the CP formalism can be used to analyze and study the establishment of MVB in two chalcogenides, GeSe and PbSe, in a similar fashion as the electron localization function (ELF) profiles. This is accomplished by analyzing the CP maps of these two chalcogenides at different pressures (up to 40 GPa for GeSe and 10 GPa for PbSe). The CP maps show distinctive features related to the MVB, providing insights into the existence of such chemical interaction in the crystal structure of the two compounds. Similar to ELF profiles, CP maps can visualize and track the strength of the MVB in GeSe and PbSe under pressure.

1 Introduction

The chemical bond concept in inorganic crystal structures has been studied extensively by different theories and formalisms over recent years.[1–8] In quantum mechanics, the chemical bond term is still an elusive concept due to the fact that the bond's existence is not directly observable in itself.[9] It can be indirectly detected from variables such as bond enthalpies, interatomic distances, and electron density maps. Since understanding the bonding nature becomes a need to design and synthesis of new materials, it is essential to devise new tools to understand chemical bonds.

Great effort is being invested in developing new density functional theory (DFT)-based approaches to visualize and analyze chemical bonds. In general, the quantum mechanical approaches are based on (1) extracting bonding features from wave functions,[10–19] electron density [Bader's quantum theory of atoms in molecules (QTAIM)],[20,21] density matrices,[4,22–27] or derivative functions,[28–34] or (2) the total-energy decomposition into several terms with physical meaning.[35–38] These two approaches are merged in a newly developed formalism, the DFT-Chemical Pressure (CP),[39] which is able to identify and visualize the chemical bond in terms of the attractive and repulsive forces located between the atoms.

The DFT-CP method has been widely used for several purposes, *e.g.*, to analyze chemical bonds,[40] to visualize the formation and rupture of bonds in crystalline systems,[41] to establish a relationship between pressure and electronegativity in inorganic crystals,[42] and to provide deep insights of the valence shell electron pair repulsion (VSEPR) model.[43]

As mentioned above, the DFT-CP method has been used to analyze the bonding network in various inorganic crystalline systems in which different CP profiles were obtained for the different types of chemical bonds, *e.g.* covalent, ionic, metallic, and weak noncovalent interactions, such as van der Waals and hydrogen bonds.[40] However, the CP approach still has not been used to study a recently defined interatomic interaction called metavalent bond (MVB).

MVB has been well defined by combining the theoretical and experimental bonding descriptors as a kind of bonding intermediate between covalent and metallic bonding.[44–52] The quantum mechanical descriptor of this bond is defined in the (de-)localization of the valence electrons along the atomic contacts. In this context, the electron localization function (ELF) approach has been widely used to investigate the chemical bond and to identify the electronic descriptor. On the other hand, the experimental bond descriptors can be extracted from measurable variables, such as the Born effective charge (Z^*), the optical dielectric constant (ε_∞), the effective coordination number (ECON), the electrical conductivity (σ) and the optical band gap (E_g). It has been shown that materials

[a] *Chemistry Department, Faculty of Science, Helwan University, Ain-Helwan, 11795, Cairo, Egypt. E-mail: hokashif@science.helwan.edu.eg*
[b] *Instituto de Diseño para la Fabricación y Producción Automatizada, MALTA Consolider Team, Universitat Politècnica de València, 46022 Valencia, Spain*

† Electronic supplementary information (ESI) available. See DOI: https://doi.org/10.1039/d2cp00954d

exhibiting MVB have significantly different descriptors compared to the conventional covalent, ionic, and metallic chemical bonds, so they have been proposed to be named *incipient metals*.[47]

MVB has been shown to be present in a number of group-14 and −15 chalcogenides, like GeTe, SnTe, PbS, PbSe, PbTe, Sb_2Te_3, Bi_2Se_3, Bi_2Te_3, $AgSbTe_2$, $Ge_2Sb_2Te_5$[53] and several mixed chalcogenides, like $SnSb_2Te_4$,[48] at room pressure (RP), as well as in the high-pressure (HP) phases of GeSe,[44,54] and As_2S_3.[55] Interestingly, GeSe and As_2S_3, as well as many other group-14 and −15 chalcogenides, like GeS, SnS, SnSe, As_2Se_3, As_2Te_3, Sb_2S_3, Sb_2Se_3, and Bi_2S_3, show covalent bonds at RP and satisfy the octet rule at RP as 8-electron compounds or A^NB^{8-N} compounds. In addition, the influence of MVB on optical and electrical properties of selected pseudo-binary compounds such as $GeTe_{1-x}Se_x$, $Sb_2Te_{3(1-x)}Se_{3x}$, and $Bi_{2-2x}Sb_{2x}Se_3$ have shown a change from covalent to metavalent bonding depending on the composition.[56] Notably, chalcogenides showing MVB do not satisfy the octet rule at RP because they crystallize in structures having much larger cation coordination than chalcogenides featuring covalent bonds. This means that 10-electron compounds or A^NB^{10-N} compounds, like IV–VI materials, have two different behaviors.[57,58] Some satisfy the octet rule and show covalent bonds due to considerable s–p hybridization, while others do not satisfy the octet rule and show a kind of p-type resonant bonds.

In most A^NB^{10-N} compounds, like GeTe, SnTe, and Pb chalcogenides, each atom is octahedrally coordinated to six neighbors, despite the average number of valence electrons for each atom being three p electrons. This means they form six bonds despite having electrons to form only three covalent p-bonds as it happens in A^NB^{8-N} compounds, like GeS, GeSe, SnS, and SnSe. Therefore, the three p-bonds have to be resonant among the six neighbors in A^NB^{10-N} compounds in order to stabilize the lattice.[57,58] This bonding mechanism has been recently called MVB because A^NB^{10-N} compounds have very different properties from those present in common A^NB^{8-N} compounds.[48]

As already commented, the establishment of MVB in some A^NB^{10-N} compounds at RP and in some A^NB^{8-N} compounds at HP has been described with the help of ELF.[44,48,55] In particular, notable changes in the ELF have been found on changing from the covalent to the metavalent bonding at HP in GeS, GeSe, PbSe, and As_2S_3.[44,55] In this article, we will take as a case of study the covalent and metavalent bondings of GeSe and PbSe at different pressures as done in ref. 44, but from the point of view of CP formalism. For that purpose, the CP profiles of GeSe and PbSe have been calculated at different pressures and compared to the corresponding ELF profiles. In that way, we will show that CP can detect the strength of the MVB in both systems similarly to ELF. As the covalent character increases, ELF attractor value increases (*e.g.* ELF well depth decreases), and CP minima decrease (CP becomes more negative and the well depth increases). Therefore, we will show that the CP and ELF formalisms are equivalent in order to describe both the covalent and metavalent bonds of these two compounds at different pressures.

2 Technical details

Crystal structure

In this work, we study two IV–VI compounds, GeSe and PbSe at different pressures from the chemical point of view with the help of *ab initio* calculations. These two different A^NX^{10-N} compounds behave in a completely different way under pressure. GeSe crystallizes in the orthorhombic *Pmcn* (GeS-type) structure at ambient pressure and shows three relatively strong covalent Ge–Se bonds. At HP, GeSe undergoes a phase transition in the range of 25–35 GPa and it completely transforms to the TlI-type orthorhombic structure (no. 63, *Ccmm*) at 40 GPa, thus increasing Ge coordination from three to five.[44] This change causes the disappearance of two of the three covalent bonds and the appearance of four MVB. On the contrary, PbSe crystallizes in the rock-salt structure at RP and shows six MVBs. At HP, PbSe undergoes a phase transition to the TlI-type orthorhombic structure at *ca.* 4 GPa, thus decreasing Pb coordination from six to five.[44] This change causes the disappearance of two of the six MVBs and the appearance of one covalent bond. This means that, in both GeSe and PbSe, the TlI-type structure is composed of square pyramidal units with four equal MVBs on each quadrilateral base and one covalent bond along the *c* direction perpendicular to the layered planes. In summary, HP establishes the MVB in GeSe, but downgrades it in PbSe. Our calculations will show that the CP formalism is equivalent to the ELF formalism in order to describe the metavalent bonding in both compounds.

Computational details

Herein, first-principles total energy electronic structure calculations were performed on GeSe and PbSe. The local density approximation (LDA) exchange–correlation functional of Goedecker, Teter, and Hutter[59] and Hartwigsen–Goedecker–Hutter norm-conserving pseudopotentials[60] were used under the formalism of density functional theory (DFT) as implemented in the ABINIT software package.[61–63] The geometrical optimization of the unit cells was performed with the Broyden–Fletcher–Goldfarb–Shanno minimization algorithm. The structural relaxation was carried out until the maximal forces on the atoms were less than 5×10^{-5} Ha $bohr^{-1}$. Dense Monkhorst–Pack *k*-point grids[64] were used to ensure the convergence of the total energy within 10^{-4} Ha per atom. A cutoff energy of 100 Ha was used in all the calculations. *k*-Point meshes of $8 \times 8 \times 3$ and $8 \times 8 \times 8$ were set for the orthorhombic and rock-salt systems, respectively. The optimized lattice parameters of GeSe and PbSe under different pressures are summarized in Tables S1 and S2 of the ESI.†

DFT calculations were performed at two different pressure ranges, 0–40 GPa and 0–10 GPa for GeSe and PbSe, respectively. In the case of the orthorhombic GeSe phase, full structure relaxation over a pressure range from 0 to 40 GPa was carried out. In contrast, and since the first-order transition of PbSe is not achievable in DFT simulations because both phases are stable over the entire pressure range (0–10 GPa); *e.g.*, the atomic positions and cell shapes of both phases do not change in this

range, the calculations were performed on the two phases of PbSe: rocksalt at 0 GPa and orthorhombic at 10 GPa.

The raw data for the CP program are prepared as three single-point calculations over a volume change of 0.5% around the equilibrium unit cell volume. CP maps are then created using the DFT-CP package.[65] These CP maps were found to be chemically and physically stable showing equivalent results with respect to different computational details as the choice of exchange–correlation functionals. Unless specifically noticed, all the calculations were performed using the core unwarping method in order to reduce the strong CP features around the atomic cores.[40,65] All the CP maps were visualized using VESTA program,[66] using appropriate pressure range scales for the color maps to reveal the CP features around the atomic cores and in the interatomic regions (normally red indicates the highest positive CP and blue indicates the lowest negative CP). In other words, negative pressures regions, where the electron density is ready for a reduction of volume, corresponds to attractive forces between the nuclei, while positive pressure regions correspond to indicate the repulsive forces between them. Thus, overall, we can expect negative CPs to be associated with bonds and attractive interactions, whereas positive CPs would be related to core electrons and repulsive interactions. Pressure values are given throughout the manuscript in atomic units (a.u.) unless otherwise specified (1 a.u. = 29421 GPa).

Briefly, the DFT-CP approach is based on that the total energy of a periodic DFT calculation can be expressed as an integral of the energy density (ρ_{energy}):

$$E_{\text{DFT}} = \int \rho_{\text{energy}}\, \mathrm{d}\tau + E_{\text{remainder}}$$

where the energy density (ρ_{energy}) can be extracted from the DFT calculation as the sum of the mappable terms defining kinetic, Hartree, local pseudopotential, and exchangre–correlation energy densities:

$$\rho_{\text{energy}} = \rho_{\text{kinetic}} + \rho_{\text{Hartree}} + \rho_{\text{psp}} + \rho_{\text{XC}}$$

while the remaining terms ($E_{\text{remainder}}$) that can't be mapped, are treated as a homogenous background to obtain an energy map with an overall pressure of the unit cell. The unit cell volume is partitioned into (N_{voxel}) voxels with volume (ν_{voxel}) which is associated with the grid points used in the calculations. Like the thermodynamic macroscopic pressure, the microscopic chemical pressure at each voxel is defined as the derivative of the local energy ($\varepsilon_{\text{voxel}}$) with respect to its volume (ν_{voxel}):

$$p_{\text{voxel}} = -\frac{\partial \varepsilon_{\text{voxel}}}{\partial \nu_{\text{voxel}}} = -\frac{E^{+}_{\text{voxel}} - E^{-}_{\text{voxel}}}{\nu^{+}_{\text{voxel}} - \nu^{-}_{\text{voxel}}}$$

In other words, the voxel pressure is easily determined by taking the difference of energy for that voxel in the slightly expanded (+) and contracted (–) structures.

3 Results and discussion

Chemical pressure of GeSe crystal

The orthorhombic *Pmcn* phase of GeSe at RP shows three almost equal Ge–Se bonds, one axial (AX) and two equatorial (EQ) bonds of length 2.553 and 2.535 Å, respectively. Additionally, each Ge atom has two second nearest Se neighbors at a distance of 3.267 Å and an interlayer Ge–Ge distance of 3.238 Å. Fig. 1a represents the 1D ELF profiles of different contacts within the unit cell and plotted as a function of the normalized bond distances. The ELF analysis shows two types of bonding based on the ELF attractor values between the atoms. On one hand, both AX and EQ bonds have similar electron density localization with a value of *ca.* 0.72 that reflects the covalent character of these three bonds. On the other hand, the ELF profiles between the two other contacts, the Ge–Ge and Ge–Se (2nd nearest Se, named MV distance in Fig. 1c), show significantly low ELF values reflecting almost no bond behavior in these regions (see Fig. 1b). All these ELF values in GeSe at RP are similar to those obtained in ref. 44 at 1 GPa.

A similar picture can be extracted from the CP analysis of the bonding network of the crystal. As discussed in previous works, the chemical bond is revealed by the CP approach through the attractive and repulsive forces between the atoms. In regions of negative CP, local energy is lowered by volume reduction that suggests that electrons in this region are more localized and the ions are packed too sparsely around them. In contrast, regions of positive CP, where electrons are not comfortable, would be stabilized by expanding the unit cell leading to a delocalized electron density.

The forces of attraction and repulsion in the orthorhombic GeSe at RP are manifested in the CP graphs (see Fig. 1c and d). The 1D CP profile along the possible contacts in the GeSe crystal as a function of the normalized distance are shown in Fig. 1c. They exhibit deep minima of negative CP (*ca.* –0.024 a.u.)

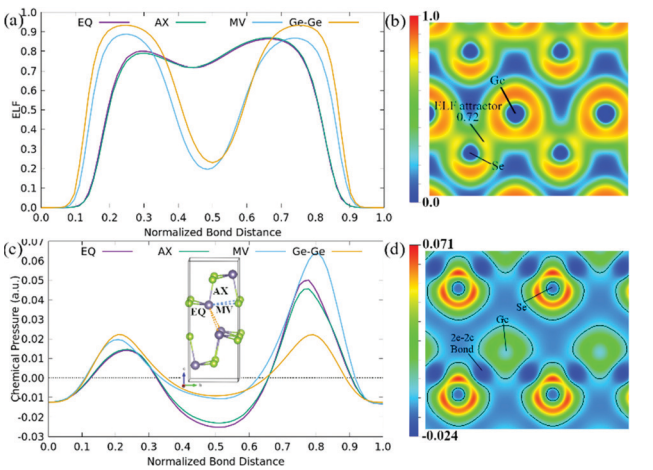

Fig. 1 ELF and chemical pressure plots of GeSe crystal (*Pmcn*) at room pressure. (a) 1D ELF, (b) 2D ELF, (c) 1D CP with an inset of the unit cell showing the main distances, and (d) 2D cross-section of the total CP map through the [001] plane. A black contour is shown for CP = 0. Chemical pressures are given in atomic units (a.u.).

along the AX and EQ Ge–Se bonds while the MV and Ge–Ge bonds have a localized negative CP region, near the half distance, of higher values (*ca.* −0.01 a.u.). A look at the 2D slice of the CP map in Fig. 1d reveals the regions of negative CP (deep blue) between the Ge and Se atoms correspond to the localization of the $2e^-$ of the covalent bond. On the other hand, flat regions of negative CP (faint blue) are distributed over the interstitial regions even along the MV contacts. These schemes show the covalent character of the bonds along the AX and EQ distances and the weak attraction forces along the other two longer distances, MV and Ge–Ge.

As pressure increases, all Ge–Se distances decrease, but large distances decrease more than short ones. For instance, AX, EQ, MV and Ge–Ge distances at 10 GPa become 2.512, 2.460, 3.006 and 2.940 Å, respectively (see Fig. S1 in the ESI†). As expected, the larger decrease of the MV distance than the AX and EQ distances leads to an increase of the ELF value (around 0.3) for the MV bond (for more details, see Fig. S2 in the ESI†). Similar behavior can be observed for the 1D CP plot, where the CP value of the MV bond goes below −0.01 a.u. (see Fig. S2 in the ESI†).

However, a different behavior occurs at pressures above 10 GPa. For instance, AX, EQ, MV, and Ge–Ge distances at 20 GPa become 2.466, 2.499, 2.809, and 2.814 Å, respectively (see Fig. S1 in the ESI†). This means that while the AX, MV, and Ge–Ge distances decrease with increasing pressure, the EQ distances now increase with increasing pressure, *i.e.*, two short covalent bonds increase in length with increasing pressure above 10 GPa. Due to the decrease of the MV distance, the ELF value of the MV bond reaches a value above 0.4 (see Fig. S3 in the ESI†). At this pressure, the ELF values of the AX and EQ bonds show different values, being the ELF value of the AX bond larger than that of the EQ bonds. This means that the strength of the EQ bonds is smaller than that of the AX bond. Similar information is obtained from the CP plot (see Fig. S3 in the ESI†). It can be observed how the CP value of the MV bond almost reaches now −0.02 a.u., *i.e.*, approaching the CP values found for AX and EQ bonds. Additionally, the CP value of the EQ bonds (larger in absolute value than that of the AX bond) is closer to that of the AX bond than at 10 GPa, thus reflecting the increase of the EQ bond distances.

As hydrostatic pressure increases to 30 GPa, the AX bond is shortened to 2.429 Å while the two EQ bonds expand to 2.511 Å. Similarly, at low pressures, the MV (2.617 Å) and Ge–Ge (2.731 Å) distances continue decreasing. The change in the bond distances is reflected in 1D plots of both ELF and CP, as shown in Fig. 2(a and c). Although the ELF attractors, in addition to CP minima, appear slightly different along the AX and EQ Ge–Se bonds, the MV and Ge–Ge bonds become stronger with higher values of ELF and negative CP than at RP. A look at the 2D CP map at 30 GPa (Fig. 2d) shows that the two local CP minima along the two EQ bonds appear with deep blue color while the other two arms of the square base, representing the MV bonds, show a little darker blue color along the direction from Ge to Se. This means that both EQ and MV bonds are very similar at this pressure.

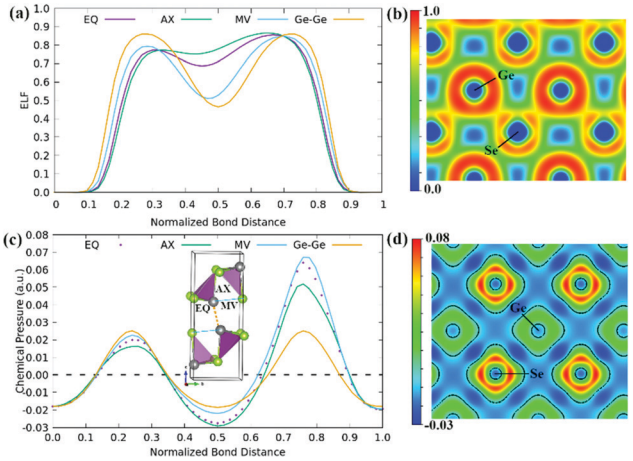

Fig. 2 ELF and chemical pressure plots of GeSe crystal (*Pmcn*) at 30 GPa. (a) 1D ELF, (b) 2D ELF, (c) 1D CP with an inset of the unit cell showing the main distances, and (d) 2D cross-section of the total CP map through the [001] plane. A black contour is shown for CP = 0.

Between 25 and 35 GPa, GeSe gradually transforms from the orthorhombic Pnma structure into a "pyramid-like" TlI-type layered structure (see inset of Fig. 3c). This structure has four equivalent equatorial Ge–Se bonds on the base of each pyramid and a fifth axial Ge–Se bond perpendicular to the basis of the pyramid. The axial bond in the TlI-type structure (AX) is similar to that of the *Pnma* phase and is covalent in nature, while the four equivalent equatorial Ge–Se bonds come from the two EQ bonds and the two MV bonds in the *Pnma* structure. The four EQ bonds in the TlI-type structure share four p electrons in a resonant way and they are the metavalent bonds, as previously described.[44–47]

The ELF and CP profiles of TlI-type GeSe at 40 GPa are shown in Fig. 3. It is clear from the 1D profiles of ELF and CP at

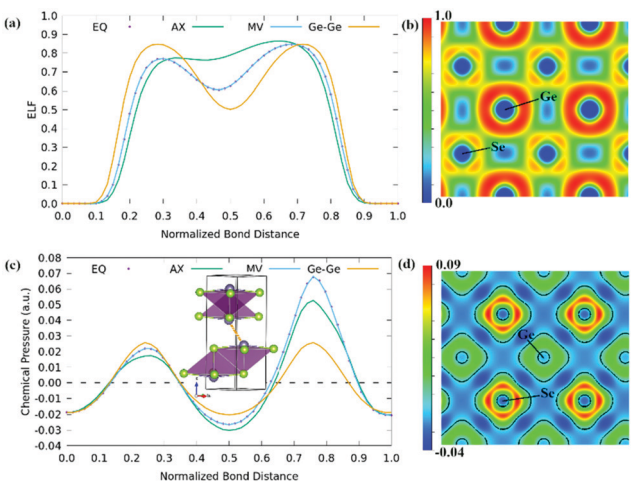

Fig. 3 ELF and chemical pressure plots of GeSe crystal (*Ccmm*) with four equivalent bonds on the base of each pyramid at 40 GPa. (a) 1D ELF, (b) 2D ELF, (c) 1D CP with an inset of the unit cell showing the polyhedra around Ge atoms, and (d) 2D cross-section of the total CP map through the [001] plane. A black contour is shown for CP = 0.

40 GPa that the AX Ge–Se bond is the shortest with higher strength in the crystal structure (high ELF + low negative CP). The values of ELF and CP are linked together to the strong covalent character of the bond. On the contrary, all the equatorial bonds (2EQ + 2MV) show precisely the same ELF value (*ca.* 0.6) near the middle point of the normalized distance between the two atoms. This value is very small for a covalent bond, and it is typical of the values found in MVB.[48,55]

A new entity appearing in the 2D CP map (see Fig. 3d) is the negative CP regions along the two arms of the MV contacts with a value *ca.* –0.025 a.u. They show exactly the same values as those of the EQ bonds and are higher than for the AX bond. Interestingly, the 2D ELF and CP maps in the equatorial plane are entirely symmetric, representing the square pyramid basis.

In summary, our study of GeSe at HP shows how this layered compound with three covalent Ge–Se bonds at RP undergoes a gradual transformation towards a layered phase with one covalent Ge–Se bond and four metavalent Ge–Se bonds. The ELF and CP formalisms are shown to be valid to describe these two bond types. More ELF and CP schemes for the orthorhombic phase of GeSe at 10 and 20 GPa can be found in the ESI† file [see Fig. S2 and S3 in the ESI†].

Chemical pressure of PbSe crystal

Now we show the opposite case, *i.e.*, a compound where pressure partially weakens the MVB. PbSe was chosen as it is a well-known thermoelectric material that is isoelectronic to GeSe. At RP, PbSe crystallizes in the cubic rock-salt structure showing six equal Pb–Se bonds of 3.003 Å. The three p orbitals of Pb atoms are not enough to establish six equivalent bonds unless electrons are shared between different bonds in a resonant way. Therefore, PbSe is a compound showing only MVB at RP.[44]

Fig. 4 shows the ELF and CP plots of the rock-salt phase of PbSe (no. 225, $Fm\bar{3}m$) at RP. An ELF attractor of a value *ca.* 0.43 is located between the two atoms that is similar to that obtained in ref. 44 and close to that obtained for the metavalent bonds in the HP phase of GeSe (*ca.* 0.6). On the other hand, a well of negative CP is detected along the Pb–Se bond with a local minimum of –0.012 a.u. that compares with the value of metavalent bonds in the HP phase of GeSe (–0.025 a.u.).

Interestingly, the 1D ELF and CP plots of PbSe are not similar to the known profiles of typical ionic materials, such as NaCl. The 1D CP plot of NaCl is characterized by a plateau region (no negative CP) between the atoms (see Fig. S4 in the ESI†). Therefore, the pure ionic bond has a non-directional plateau region of CP in the interstitial spaces. In contrast, rock-salt PbSe shows evidence of non-ionic bonding. The smaller absolute values of ELF and CP found for the MV bonds in PbSe than in GeSe are likely related to the different distribution of bonding electrons between four bonds in TlI-type GeSe and six bonds in rock-salt PbSe. Thus, based on ELF and CP analysis, it is clear that the chemical bond in rock-salt PbSe at RP is neither ionic nor pure covalent bond. In summary, the comparison between ELF and CP profiles shows that the newly developed

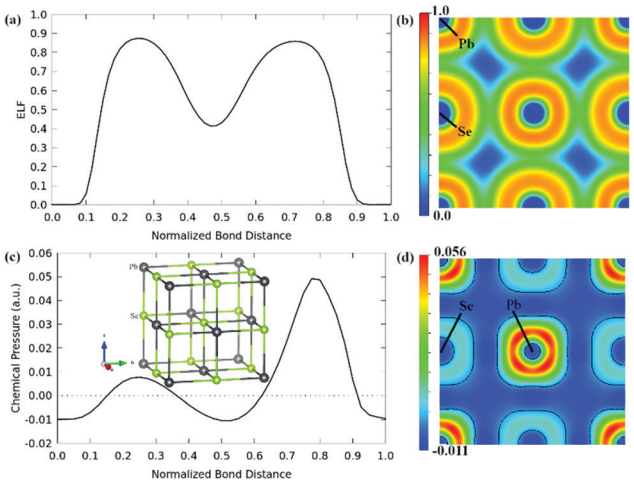

Fig. 4 ELF and chemical pressure plots of PbSe crystal ($Fm\bar{3}m$) at room pressure. 1D profile of (a) ELF and (c) CP along the normalized Ge–Se bond path with an inset of the PbSe unit cell. 2D cross-section of (b) ELF and (d) the total CP map through the [001] plane. A black contour is shown for CP = 0.

CP formalism can be used to visualize and analyse the different types of chemical bonding, including the MV bond.

At HP, PbSe gradually evolves into a ''pyramid-like'' TlI-type layered structure (see inset of Fig. 5c) above 3–4 GPa.[67,68] This structure has four equivalent equatorial Pb–Se bonds on the base of each pyramid and a fifth axial Pb–Se bond perpendicular to the basis of the pyramid. While the AX bond is covalent in nature, the four EQ bonds share four p electrons, and thus, they are metavalent bonds, as previously described.[44–47] At 10 GPa, the AX (named AX1) and EQ bond distances in the TlI-type structure of PbSe are 2.703 and 2.897 Å, respectively. When the transformation occurs, one Pb–Se bond of the

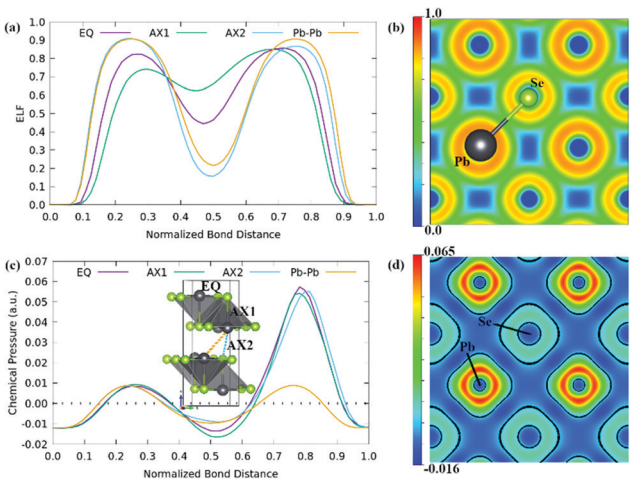

Fig. 5 ELF and chemical pressure plots of PbSe crystal (*Ccmm*) at 10 GPa. 1D profile of (a) ELF and (c) CP along the normalized Ge–Se bond path with an inset of the PbSe unit cell showing the polyhedra around Pb atoms. 2D cross-section of (b) ELF and (d) the total CP map through the [001] plane. A black contour is shown for CP = 0.

rock-salt phase (AX2 in the TlI-type structure) is lost along the axial direction (see Fig. S4 in the ESI†).

The 1D ELF plot (Fig. 5a) shows the different profiles along possible atomic contacts in the crystal structure of TlI-type PbSe at 10 GPa. An ELF attractor with a value of *ca.* 0.65 is located near the middle point of the normalized Pb–Se distance for the AX1 bond, as expected for a covalent bond. On the contrary, the AX2 bond shows a deep well of ELF (*ca.* 0.17), providing evidence for the absence of this Pb–Se bond in this structure. Also, the interlayer Pb–Pb distance shows a weak ELF, so no bond is formed. Finally, all the equatorial bonds (2EQ + 2MV) show exactly the same ELF value (*ca.* 0.48) near the middle point of the normalized distance between the two atoms. This value is very small for a covalent bond, and it is typical of the values found in MVB.[48,55] Note that similar values of ELF were provided for PbSe at 9 GPa in ref. 44.

In summary, our study of PbSe at HP shows how this 3D compound with rock-salt structure and six equivalent metavalent Pb–Se bonds at RP undergoes a gradual transformation towards a layered phase with one covalent Pb–Se bond and four metavalent Pb–Se bonds. Again, the ELF and CP formalisms are shown to be valid to describe metavalent bonds as well as covalent, ionic, metallic, van der Waals, and hydrogen bonds.

4. Conclusions

Both GeSe and PbSe have been studied theoretically under compression using the ELF and CP formalisms. While GeSe is a covalent solid at RP that becomes an incipient metal characterized by metavalent bonds at HP (typically around 35–40 GPa), PbSe is already an incipient metal at RP that losses part of the metavalent bonding at HP (typically around 3–4 GPa). It has been shown that both ELF and CP formalisms describe in a similar fashion metavalent bonds in the same way as it was previously shown for covalent, ionic, metallic, van der Waals, and hydrogen bonds. Therefore, this work allows to complete the characterization of the most known bonds with the CP formalism that will be of help to researchers in order to use the CP formalism as an equivalent of the ELF that it is much complex to calculate.

Conflicts of interest

There are no conflicts to declare.

Acknowledgements

This publication is part of the project MALTA Consolider Team network (RED2018-102612-T), financed by MINECO/AEI/10.13039/501100003329; by I+D+i project PID2019-106383GB-42, financed by MCIN/AEI/10.13039/501100011033; and by project, PROMETEO/2018/123 (EFIMAT), financed by Generalitat Valenciana.

Notes and references

1 L. Pauling, *The Nature of the Chemical Bond and the Structure of Molecules and Crystals: An Introduction to Modern Structural Chemistry*, Cornell University Press, Ithaca, New York, 1960.
2 G. N. Lewis, *Valence and the Structure of Atoms and Molecules*, Dover, New York, 1966.
3 C. Gatti, *Z. Kristallogr.*, 2005, **220**, 399–457.
4 F. Weinhold and C. R. Landis, *Valency and Bonding: A Natural Bond Orbital Donor-Acceptor Perspective*, Cambridge University Press, Cambridge, 2005.
5 M. W. Schmidt, J. Ivanic and K. Ruedenberg, in *The Physical Origin of Covalent Bonding: The Chemical Bond: Fundamental Aspects of Chemical Bonding*, ed. G. Frenking and S. Shaik, Wiley-VCH Verlag: Weinheim, Germany, 1st edn, 2014.
6 G. Frenking and S. Shaik, *The Chemical Bond: Fundamental Aspects of Chemical Bonding*, Cambridge University Press: Cambridge, UK, 2005.
7 A. Mujica, A. Rubio, A. Muñoz and R. J. Needs, *Rev. Mod. Phys.*, 2003, **75**, 863–912.
8 C. Gatti and P. Macchi, *Modern Charge Density Analysis*, ed. C. Gatti and P. Macchi, Springer, Dordrecht Heidelberg, London, New York, 2012, Springer, I ISBN 978-90-481-3835-7.
9 P. Needham, *Stud. Hist. Philos. Sci. A*, 2014, **45**, 1–13.
10 V. J. Yannello, B. J. Kilduff and D. C. Fredrickson, *Inorg. Chem.*, 2014, **53**, 2730–2741.
11 J. M. Foster and S. F. Boys, *Rev. Mod. Phys.*, 1960, **32**, 300–302.
12 K. A. Yee and T. Hughbanks, *Inorg. Chem.*, 1991, **30**, 2321–2328.
13 G. H. Wannier, *Phys. Rev.*, 1937, **52**, 191–197.
14 E. Zurek, O. Jepsen and O. K. Andersen, *Inorg. Chem.*, 2010, **49**, 1384–1396.
15 N. Marzari, A. A. Mostofi, J. R. Yates, I. Souza and D. Vanderbilt, *Rev. Mod. Phys.*, 2012, **84**, 1419–1475.
16 T. Hughbanks and R. Hoffmann, *J. Am. Chem. Soc.*, 1983, **105**, 3528–3537.
17 T. Hughbanks and R. Hoffmann, *J. Am. Chem. Soc.*, 1983, **105**, 1150–1162.
18 A. C. West, M. W. Schmidt, M. S. Gordon and K. Ruedenberg, *J. Phys. Chem. A*, 2015, **119**, 10360–10367.
19 A. C. West, M. W. Schmidt, M. S. Gordon and K. Ruedenberg, *J. Phys. Chem. A*, 2013, **139**, 234107.
20 R. F. W. Bader, *Atoms in Molecules: a Quantum Theory*, Clarendon Press, Oxford, 1990.
21 E. R. Johnson, S. Keinan, P. Mori-Sánchez, J. Contreras-García, A. J. Cohen and W. Yang, *J. Am. Chem. Soc.*, 2010, **132**, 6498–6506.
22 J. P. Foster and F. Weinhold, *J. Am. Chem. Soc.*, 1980, **102**, 7211–7218.
23 A. E. Reed and F. Weinhold, *J. Chem. Phys.*, 1985, **83**, 1736–1740.
24 A. E. Reed, L. A. Curtiss and F. Weinhold, *Chem. Rev.*, 1988, **88**, 899–926.
25 F. Weinhold and C. R. Landis, *Discovering Chemistry with Natural Bond Orbitals*, John Wiley & Sons, Inc., Hoboken, NJ, USA, 2012.
26 T. R. Galeev, B. D. Dunnington, J. R. Schmidt and A. I. Boldyrev, *Phys. Chem. Chem. Phys.*, 2013, **15**, 5022–5029.

27 J.-A. Dolyniuk, H. He, A. S. Ivanov, A. I. Boldyrev, S. Bobev and K. Kovnir, *Inorg. Chem.*, 2015, **54**, 8608–8616.
28 K. E. Becke and A. D. Edgecombe, *J. Chem. Phys.*, 1990, **92**, 5397.
29 A. Savin, A. D. Becke, J. Flad, R. Nesper, H. Preuss and H. G. von Schnering, *Angew. Chem., Int. Ed. Engl.*, 1991, **30**, 409–412.
30 A. Savin, R. Nesper, S. Wengert and T. F. Fässler, *Angew. Chem., Int. Ed. Engl.*, 1997, **36**, 1808–1832.
31 M. Kohout, K. Pernal, F. R. Wagner and Y. Grin, *Theor. Chem. Acc.*, 2004, **112**, 453–459.
32 A. Savin, *THEOCHEM*, 2005, **727**, 127–131.
33 B. Silvi and A. Savin, *Nature*, 1994, **371**, 6499.
34 F. R. Wagner, V. Bezugly, M. Kohout and Y. Grin, *Chem. – Eur. J.*, 2007, **13**, 5724–5741.
35 M. V. Hopffgarten and G. Frenking, *Wiley Interdiscip. Rev.: Comput. Mol. Sci.*, 2012, **2**, 43–62.
36 R. Dronskowski and P. E. Bloechl, *J. Phys. Chem.*, 1993, **97**, 8617–8624.
37 A. C. West, M. W. Schmidt, M. S. Gordon and K. Ruedenberg, *J. Phys. Chem. A*, 2017, **121**, 1086–1105.
38 F. Wang and G. J. Miller, *Inorg. Chem.*, 2011, **50**, 7625–7636.
39 D. C. Fredrickson, *J. Am. Chem. Soc.*, 2011, **133**, 10070–10073.
40 H. H. Osman, M. A. Salvadó, P. Pertierra, J. Engelkemier, D. C. Fredrickson and J. M. Recio, *J. Chem. Theory Comput.*, 2018, **14**, 104–114.
41 H. Osman, J. Andrés, M. Salvadó and J. M. Recio, *J. Phys. Chem. C*, 2018, **122**, 21216–21225.
42 Á. Lobato, H. H. Osman, M. A. Salvadó, P. Pertierra, Á. Vegas, V. G. Baonza and J. M. Recio, *Inorg. Chem.*, 2020, **59**, 5281–5291.
43 A. Lobato, H. H. Osman, M. A. Salvadó, M. Taravillo, V. G. Baonza and J. M. Recio, *Phys. Chem. Chem. Phys.*, 2019, **21**, 12585–12596.
44 M. Xu, S. Jakobs, R. Mazzarello, J.-Y. Cho, Z. Yang, H. Hollermann, D. Shang, X. Miao, Z. Yu, L. Wang and M. Wuttig, *J. Phys. Chem. C*, 2017, **121**, 25447–25454.
45 M. Zhu, O. Cojocaru-Mirédin, A. M. Mio, J. Keutgen, M. Küpers, Y. Yu, J.-Y. Cho, R. Dronskowski and M. Wuttig, *Adv. Mater.*, 2018, **30**, 1706735.
46 J.-Y. Raty, M. Schumacher, P. Golub, V. L. Deringer, C. Gatti and M. Wuttig, *Adv. Mater.*, 2019, **31**, 1806280.
47 M. Wuttig, V. L. Deringer, X. Gonze, C. Bichara and J.-Y. Raty, *Adv. Mater.*, 2018, **30**, 1803777.
48 J. A. Sans, R. Vilaplana, E. L. da Silva, C. Popescu, V. P. Cuenca-Gotor, A. Andrada-Chacón, J. Sánchez-Benitez, O. Gomis, A. L. J. Pereira, P. Rodríguez-Hernández, A. Muñoz, D. Daisenberger, B. García-Domene, A. Segura, D. Errandonea, R. S. Kumar, O. Oeckler, P. Urban, J. Contreras-García and F. J. Manjón, *Inorg. Chem.*, 2020, **59**, 9900–9918.
49 C. Bellin, A. Pawbake, L. Paulatto, K. Béneut, J. Biscaras, C. Narayana, A. Polian, D. J. Late and A. Shukla, *Phys. Rev. Lett.*, 2020, **125**, 145301.
50 S. Maier, S. Steinberg, Y. Cheng, C.-F. Schön, M. Schumacher, R. Mazzarello, P. Golub, R. Nelson, O. Cojocaru-Mirédin, J.-Y. Raty and M. Wuttig, *Adv. Mater.*, 2020, **32**, 2005533.
51 Y. Cheng, S. Wahl and M. Wuttig, *Phys. Status Solidi RRL*, 2021, **15**, 2000482.
52 D. Giri, L. Williams, A. Mukherjee and K. Rajan, *J. Chem. Phys.*, 2021, **154**, 124105.
53 B. J. Kooi and M. Wuttig, *Adv. Mater.*, 2020, **32**, 1908302.
54 D. Sarkar, S. Roychowdhury, R. Arora, T. Ghosh, A. Vasdev, B. Joseph, G. Sheet, U. V. Waghmare and K. Biswas, *Angew. Chem., Int. Ed.*, 2021, **60**, 10350–10358.
55 V. P. Cuenca-Gotor, J. Á. Sans, O. Gomis, A. Mujica, S. Radescu, A. Muñoz, P. Rodríguez-Hernández, E. L. da Silva, C. Popescu, J. Ibañez, R. Vilaplana and F. J. Manjón, *Phys. Chem. Chem. Phys.*, 2020, **22**, 3352–3369.
56 L. Guarneri, S. Jakobs, A. von Hoegen, S. Maier, M. Xu, M. Zhu, S. Wahl, C. Teichrib, Y. Zhou, O. Cojocaru-Mirédin, M. Raghuwanshi, C.-F. Schön, M. Drögeler, C. Stampfer, R. P. S. M. Lobo, A. Piarristeguy, A. Pradel, J.-Y. Raty and M. Wuttig, *Adv. Mater.*, 2021, **33**, 2102356.
57 P. B. Littlewood, *J. Phys. C: Solid State Phys.*, 1980, **13**, 4855–4873.
58 P. B. Littlewood, *Crit. Rev. Solid State Mater. Sci.*, 1983, **11**, 229–285.
59 S. Goedecker, M. Teter and J. Hutter, *Phys. Rev. B: Condens. Matter Mater. Phys.*, 1996, **54**, 1703–1710.
60 C. Hartwigsen, S. Goedecker and J. Hutter, *Phys. Rev. B: Condens. Matter Mater. Phys.*, 1998, **58**, 3641–3662.
61 X. Gonze, *Z. Kristallogr. - Cryst. Mater.*, 2005, **220**, 558–562.
62 X. Gonze, B. Amadon, P.-M. Anglade, J.-M. Beuken, F. Bottin, P. Boulanger, F. Bruneval, D. Caliste, R. Caracas, M. Côté, T. Deutsch, L. Genovese, P. Ghosez, M. Giantomassi, S. Goedecker, D. R. Hamann, P. Hermet, F. Jollet, G. Jomard, S. Leroux, M. Mancini, S. Mazevet, M. J. T. Oliveira, G. Onida, Y. Pouillon, T. Rangel, G.-M. Rignanese, D. Sangalli, R. Shaltaf, M. Torrent, M. J. Verstraete, G. Zerah and J. W. Zwanziger, *Comput. Phys. Commun.*, 2009, **180**, 2582–2615.
63 X. Gonze, F. Jollet, F. Abreu Araujo, D. Adams, B. Amadon, T. Applencourt, C. Audouze, J.-M. Beuken, J. Bieder, A. Bokhanchuk, E. Bousquet, F. Bruneval, D. Caliste, M. Côté, F. Dahm, F. da Pieve, M. Delaveau, M. di Gennaro, B. Dorado, C. Espejo, G. Geneste, L. Genovese, A. Gerossier, M. Giantomassi, Y. Gillet, D. R. Hamann, L. He, G. Jomard, J. Laflamme Janssen, S. le Roux, A. Levitt, A. Lherbier, F. Liu, I. Lukačević, A. Martin, C. Martins, M. J. T. Oliveira, S. Poncé, Y. Pouillon, T. Rangel, G.-M. Rignanese, A. H. Romero, B. Rousseau, O. Rubel, A. A. Shukri, M. Stankovski, M. Torrent, M. J. van Setten, B. van Troeye, M. J. Verstraete, D. Waroquiers, J. Wiktor, B. Xu, A. Zhou and J. W. Zwanziger, *Comput. Phys. Commun.*, 2005, **205**, 106–131.
64 H. J. Monkhorst and J. D. Pack, *Phys. Rev. B: Solid State*, 1976, **13**, 5188–5192.
65 V. M. Berns, J. Engelkemier, Y. Guo, B. J. Kilduff and D. C. Fredrickson, *J. Chem. Theory Comput.*, 2014, **10**, 3380–3392.
66 K. Momma and F. Izumi, *J. Appl. Crystallogr.*, 2011, **44**, 1272–1276.
67 S. Wang, C. Zang, Y. Wang, L. Wang, J. Zhang, C. Childs, H. Ge, H. Xu, H. Chen, D. He and Y. Zhao, *Inorg. Chem.*, 2015, **54**, 4981–4989.
68 S. V. Ovsyannikov, V. V. Shchennikov, A. E. Kar'kin and B. N. Goshchitskii, *J. Phys.: Condens. Matter*, 2005, **17**, S3179–S3183.

